

Realization of Singular Topological Edge States in Locally Resonant Metamaterials

Yeongtae Jang,^{1,*} Seokwoo Kim,^{1,*} Eunho Kim,^{2,3,†} and Junsuk Rho^{1,4,5,6,‡}

¹*Department of Mechanical Engineering, Pohang University of Science and Technology (POSTECH), Pohang 37673, Republic of Korea[‡]*

²*Division of Mechanical System Engineering, Jeonbuk National University, Jeonju, 54896, Republic of Korea[†]*

³*Department of JBNU-KIST Industry-Academia Convergence Research, Jeonju, 54896, Republic of Korea*

⁴*Department of Chemical Engineering, Pohang University of Science and Technology (POSTECH), Pohang 37673, Republic of Korea*

⁵*Department of Electrical Engineering, Pohang University of Science and Technology (POSTECH), Pohang 37673, Republic of Korea*

⁶*POSCO-POSTECH-RIST Convergence Research Center for Flat Optics and Metaphotonics, Pohang 37673, Korea*
(Dated: May 24, 2024)

We theoretically and experimentally demonstrate singular topological edge states in a locally resonant metamaterial with a configuration based on inversion-symmetric extended Su-Schrieffer-Heeger chains. Such states arise from a topological gap transition from a conventional Bragg-type gap (BG) to a local resonance-induced gap (LRG), accompanied by a topological phase transition. Remarkably, nontrivial topological states can emerge in the vicinity of the singularity in the imaginary parts of the wavenumber within the bandgap, leading to highly localized modes on a scale comparable to a single subwavelength unit cell. We experimentally demonstrate distinct differences in topologically protected modes—highlighted by wave localization—between the BG and the LRG in locally resonant granular-based metamaterials. Our findings suggest the scope of topological metamaterials may be extended via their bandgap nature.

Metamaterials have attracted attention because of their unusual effective material properties, which include zero [1, 2] and negative [3, 4] quantities, which are achieved through structural engineering using an array of unit building blocks [5–7]. The key feature of a metamaterial involves the strong coupling between local resonance and propagating Bloch modes, which permits sub-wavelength functionalities. This local resonance leads to the formation of a resonance-induced bandgap (LRG) [4]. Indeed, the dispersion of local resonance is analogous to polaritons—an anti-crossing between the propagating waves within the host medium and the resonance of the unit cell [8, 9]. Accordingly, the *gap properties* within the LRG, resulting from resonant coupling, exhibit strong wave attenuation, in contrast to the Bragg interference-induced bandgap (BG) determined by periodic modification. To realize such resonance, diverse design principles have been proposed and successfully applied in the fields of photonics [3, 5], and phononics [4, 6, 7].

Recently, the concept of band topology has emerged as a new design strategy for metamaterials. The fundamental idea of the band topology is to characterize the band structure of the *bulk* system and anticipate the behavior of *local boundaries* in their finite counterparts [10–12]. This bulk-boundary correspondence [13] has emerged as a new degree of freedom for designing metamaterials with intriguing energy localization features on their corners, edges, and surfaces [14–26]. These “in-gap” eigenstates of finite systems are determined by the specific symmetries and gap properties (i.e., the imaginary part of the wavevectors) assigned to them. What makes this special is that the topological nature of the bulk ensures robustness to the boundaries [27]. This character-

istic of topology opens up potential applications in optical, phononic, and mechanical computing [28–30], energy harvesting [30], and signal processing applications, among others [31, 32].

By combining a locally resonant metamaterial and topology, previous studies have successfully reported the emergence of topological states—from 1D locally resonant Su-Schrieffer-Hegger (SSH) [33–36] models to 2D crystalline-based metamaterials [9, 25, 37–40]. Introducing local resonances enables the realization of subwavelength topological states and the ability to tune topological mode frequencies by controlling the resonators of the constituent metamaterials. However, in most studies, the role of local resonance is merely to lower the band frequency, and the topological in-gap states still rely on the subwavelength BGs. To date, implementing a nontrivial topological phase in LRGs has remained challenging. The primary reason is that LRG, arising from the single local resonance, exhibits singularities in its gap where the effective parameters diverge, thereby preventing the gap closing required for band inversion [33].

From this perspective, we asked the following question: *How can one achieve nontrivial topological states within LRGs?* Since the in-gap state relies on the bandgap properties, the edge state within the LRG is expected to exhibit strong localization. This potential could hold significant value across various domains of physics, from photonics to mechanics and acoustics.

In this study, we uncover the fundamental mechanism behind achieving a topological state in the LRG within subwavelength regimes. The singular topological edge state embedded in an LRG exhibits extreme wave localization characteristics, significantly diverging from the

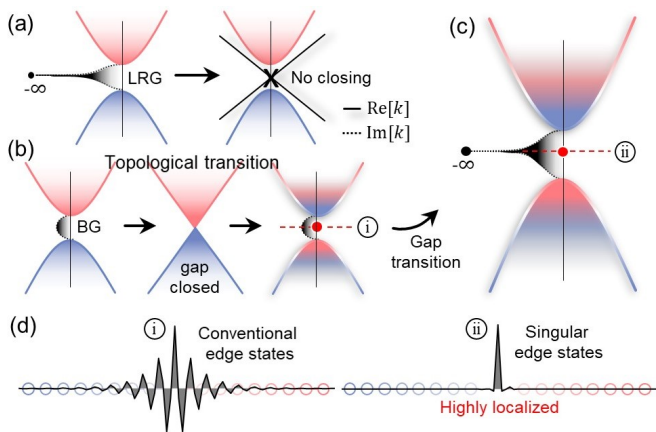


FIG. 1. Singular topological edge state. (a) Conventional local resonance-based SSH chains configured by dimerized hopping exhibit singularities in their gap, thereby preventing gap closure [33]. Our proposal is a topological band with a local resonance gap (LRG) as the reference, and is achieved through a two-step process. (b) The general topological phase transition with the Bragg-type gap (BG) as the reference. (c) Gap transition from BG to LRG. As a result of disparities in gap properties, unique topological edge states, referred to as a singular edge state, can emerge. (d) Eigenstate of topologically protected conventional edge states (within BGs) and singular edge states (within LRGs).

conventional edge state in the BG, particularly on a scale comparable to a single subwavelength unit cell. These marked differences in wave localization between the BGs and the LRGs were experimentally verified using locally resonant granular-based metamaterials.

The underlying concept of our proposal is schematically depicted in Fig. 1. As noted earlier, the general strategy for achieving topological phase transitions through dimerized configurations (e.g., SSH chain) does not lead to band closure in LRGs due to their singularity in the gap [see Fig. 1(a)]. To address this challenge, we utilize a bi-local resonance frequency instead of dimerization of the hopping. With this configuration, the transition can induce not only a topological phase [Fig. 1(b)] but also a bandgap [Fig. 1(c)]. With this process, we can achieve a topological band structure with the LRG as a reference. Interestingly, as a result of the singularity in the LRG [see Fig. 1(c)], we were able to achieve a unique topological edge state, referred to as a “singular” edge state, based on the principle of bulk-boundary correspondence. This remarkable wave localization feature in finite systems is shown in Fig. 1(d) compared to conventional edge states.

Results and discussions: Extended SSH chain—In what follows, we introduce an inversion-symmetric extended SSH chain without local resonance. The inversion symmetry plays a major role in achieving a nontrivial topology, even in the presence of broken chiral symmetry in our systems [41, 42]. Moreover, the inversion sym-

metry, even when extended to the subwavelength locally resonant system, holds significant implications for characterizing the band topology, a discussion to be addressed later. As shown in Fig. 2(a), we consider a 1D four-band mechanical lattice where the unit cell comprises four sublattices exhibiting inversion symmetry relative to the center of the unit cell. Each sublattice mass is connected by constant stiffness t . By invoking the Bloch-Floquet condition, the equations of motion for our unit cell yield an eigenvalue problem

$$[\mathcal{H}_s(k) - \omega^2 \mathcal{H}_m] |\hat{\mathbf{u}}\rangle = 0. \quad (1)$$

Here, \mathcal{H}_m and \mathcal{H}_s are Hermitian matrices composed of mass and spring constants, respectively (see Ref. [43], Sec. I.1); $|\hat{\mathbf{u}}\rangle = [u_1 \ u_2 \ u_3 \ u_4]^T$ is the displacement vector of each site; k is the wavenumber. Fig. 2(b) shows the parametric band diagram calculated from the Hamiltonian ($\mathcal{H} = \mathcal{H}_m^{-1} \mathcal{H}_s$) as a function of the mass difference $\Delta m_0 = m_b^0 - m_g^0$. Because of the inversion-symmetric mass distribution in the unit cells, the bulk Hamiltonian conserves inversion (\mathcal{R}) symmetry, i.e., $\mathcal{R}\mathcal{H}(k)\mathcal{R}^{-1} = \mathcal{H}(-k)$. For a four-band system, the inversion symmetry can be defined by the unitary operator $\mathcal{R} = \sigma_x \otimes \sigma_x$. Thus, without loss of generality, we can define \mathbb{Z}_2 topological invariant ν^n as $(-1)^{\nu^n} = \xi_0^n \xi_\pi^n = \pm 1$ [44], where n is the band index and ξ_k is the eigenvalue of the inversion operator at the time-reversal symmetric point of the Brillouin zone. The index indicates the parity of modes for each band [*even*-blue and *odd*-red; see Fig. 2(b)], determined from the eigenvalues of the inversion operators. The topological phase transition (mixed parities) occurs depending on the sign of Δm_0 . Thus, the system has two well-defined Dirac points (DPs) at momentum $k_x = \pi$ when $\Delta m_0 = 0$ [see Fig. 2(a)]. To understand the underlying physics of the energy band, we employ a perturbative approach to derive the effective Hamiltonian near the DPs. Through a unitary transformation, we can map it to the form of a massive Dirac Hamiltonian $\hat{\mathcal{H}}$ [45]; see Ref. [43], Sec. I.2 for the detailed derivation.

$$\begin{aligned} \hat{\mathcal{H}}(k) &= \frac{\sqrt{2}}{8m_0\omega_0} \begin{bmatrix} -\eta\Delta m_0\omega_0^2 & it\Delta k \\ -it\Delta k & \eta\Delta m_0\omega_0^2 \end{bmatrix} \\ &= \frac{\sqrt{2}}{8m_0\omega_0} (t\Delta k\sigma_y \pm \Delta m_0\omega_0^2\sigma_z), \end{aligned} \quad (2)$$

where ω_0 is the eigenfrequency at degeneracy, with $\eta = \mp 1$ for DPs_{1,2}. In this analogy, the diagonal element of the Hamiltonian—often called the Dirac mass—depends on the sign of Δm_0 and η . For the topological phase, our attention is on the off-diagonal element—Dirac velocity—exhibiting odd behavior in momentum space. This indicates coupling between different parities and is consistent with the results of the parametric band diagram as shown in Fig. 2(b).

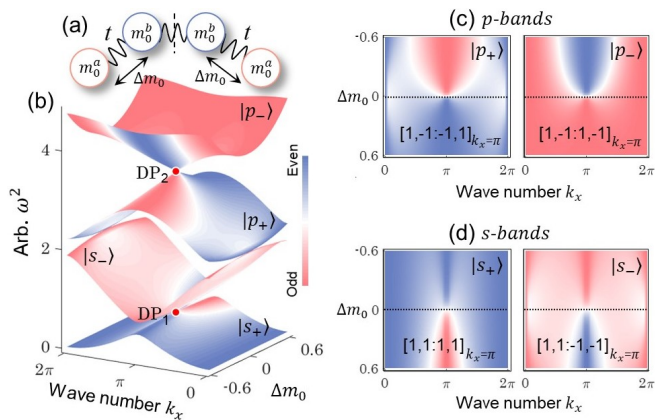


FIG. 2. Topological phase transition in the inversion-symmetric extended Su-Schrieffer-Hegger chain. (a) Representative mass-modulated (Δm_0) unit cell. (b) Parametric band diagram as a function of mass difference ($\Delta m_0 = m_0^b - m_0^a$), defining orbital $|s_{\pm}\rangle$ for the lower two bands and $|p_{\pm}\rangle$ for the upper two bands. Index denotes mode parity for each band calculated from the eigenvalue of the inversion operators. (c)-(d) s - and p -orbital with each band.

To characterize the shape of the eigenmodes in terms of symmetry (namely, orbital), we introduce a sublattice inversion operator $\mathcal{R}_s = \mathbf{I} \otimes \sigma_x$, switching positions in inversion symmetric pairs. The resulting orbitals are labeled in each band [see Fig. 2(b)]. The $|s(p)\rangle$ represent positive (negative) eigenvalues of \mathcal{R}_s and the $+(-)$ index is the eigenvalue of inversion symmetry. In Figs. 2(c)-(d), we summarize the calculated eigenvalues of the inversion operator with each band when $\Delta m_0 > 0$. when $\Delta m_0 < 0$, this eigenvalue within each p and s band is flipped through band inversion. Hence, despite the breaking of the well-known chiral symmetry, our attained inversion symmetry, enabled by a modulated mass distribution in the unit cell, can demonstrate a topologically nontrivial phase.

Locally resonant system—Next, we construct a sub-wavelength lattice—a theoretical model of the sonic metamaterials [7]—by introducing an internal resonator while maintaining the inversion-symmetric configurations. Specifically, we investigate *single*-frequency and *bi*-frequency scenarios through mass modulation while maintaining constant hopping t and the local stiffness of resonators k_1 , as shown in Figs. 3(a)-(b). The effective mass of the unit cell, expressed as $M_{\text{eff}}(\omega) = m_0 + m_1 \omega_1^2 / (\omega_1^2 - \omega^2)$, exhibits frequency-dependent behavior, where $\omega_1 = \sqrt{k_1/m_1}$ (see Ref. [43], Sec. II.1). Thus, effective masses can approach infinity at their resonant frequency. In Fig. 3(c), we show the parametric band diagram related to γ , with the host mass m_0 denoted as $1+\gamma$ and $1-\gamma$. Unless explicitly noted, parameters default to 1. Introducing a local resonator to the sublattice expands the four bands to eight (i.e., doubling the bands). The anti-crossing arising from the local reso-

nance creates LRG (gray box) at a single frequency since $\omega_1^a = \omega_1^b = 1$. Here, LRG cannot be closed regardless of the gamma, while the remaining gap (BGs) undergoes a gap-close-reopen process (i.e., a topological phase transition). Therefore, the LRG still cannot be a topological bandgap. In the subwavelength regimes ($\omega < \omega_1^{a,b}$), we observe a mode parities pattern similar to the previous inversion-symmetric SSH chain [see Fig. 2(b) and Fig. 3(d)].

Moving on, as presented in Fig. 3(e), we examine the band diagram of a bi-frequency topological chain with attention to subwavelength regimes below the LRG. In this context, the local resonance frequency of the sublattice can be tuned by adjusting the local mass ($m_1^{a,b}$) while preserving the inversion symmetry of unit cells, (i.e., $\omega_1^a = 1/\sqrt{1+\gamma}$ and $\omega_1^b = 1/\sqrt{1-\gamma}$). The parity of modes for each subwavelength band seems similar to that of the previous single-frequency topological chain. However, while the local resonance frequency remains constant in the single-frequency setup, it varies with γ in the bi-frequency configuration. We can see that the topological phase transition occurs in the subwavelength BG between the third and fourth bands when $\gamma < 0$ [see Fig. 3(e)]. With a gradual variation in γ , an intriguing observation unfolds: one of the local resonance frequencies (ω_1^b) begins to *penetrate* into a subwavelength topological gap. Upon penetration of the local resonance frequency, a topological bandgap transition occurs from the BG to LRG. In addition, this gap transition accompanies the orbital transition of the upper topological band, i.e., from $|p\rangle$ to $|s\rangle$ of the fourth bands [see Figs. 3(d)-(e)] since the effective mass for b -sublattice (m^b) becomes negative (i.e., the inversion of the sublattice symmetry).

To characterize the topological phase together with the type of bandgap, we introduce a physical quantity $\Delta\Phi \equiv \Phi_0 - \Phi_\pi$, where Φ_k is $\text{sign}(u_1/u_3)$. This quantity allows us to consider not only the inversion eigenvalue, directly linked to the topological invariant but also the orbital information. Thus, this quantity provides evidence for the bandgap transition. Fig. 3(f) shows the boundary line obtained by calculating $\Delta\Phi$ for the entire band structure (see Ref. [43], Sec. II.2) in the parametric space of the bi-frequency resonance. Within the boundary map obtained from the topological phase, the red areas represent regions where topologically nontrivial bands undergo orbital transitions. The color-index lines denote the findings of the bi-local resonator in the model used in Fig. 3(b). This penetration from BG to the LRG when $\gamma < 0$ corresponds to the bandgap transition discovered in Fig. 3(e). In addition, we investigate the spectral ordering in Ref. [43], Sec. II.3, which demonstrates gap transitions via the identical mechanism.

Based on the bulk-boundary correspondence, the topological LRG displays singular edge states, which are attributed to the singularity in the imaginary part of the wavenumber. The localization (\mathcal{P}) of the topological edge

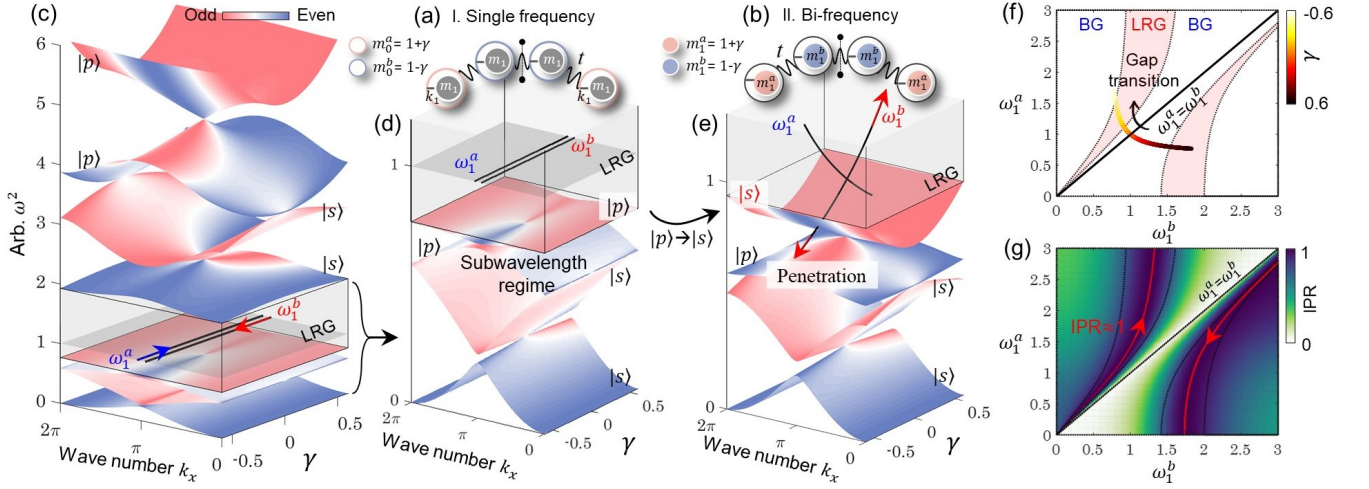


FIG. 3. Parametric band diagram in locally resonant metamaterials. (a) Single-frequency case and (b) Bi-frequency case, both maintaining the inversion symmetry of the unit cell. (c) Full eight-band structure in the single-frequency configuration. Subwavelength regimes (four bands, $\omega < \omega_1^{a,b}$) of (d) single-frequency and (e) bi-frequency configuration. Tuning the parameters of the internal resonators in the bi-frequency case allows the local resonance to penetrate the Bragg-induced gap (i.e., a gap transition occurs). (f) The boundaries obtained by calculating phase maps for the entire bands; see the main text for details. The red region indicates an embedded space where the topological bandgap is governed by the LRG rather than BG. The inset color represents the gap transition of the proposed model (i.e., $m_1^{a,b} = 1 \pm \gamma$) (h) Localization index (IPR) map in the parametric space of local resonant frequencies, where red lines depict exact singular topological edge states.

state within BG relies on the ratio of two distinct parameters, expressed as $\mathcal{P} \propto \ln(c_a/c_b)$ [46]. The $c_{a,b}$ can be either mass or stiffness. Hence, a realization of the highly localized waves—where energy is confined to a few unit cells—within this BG is unattainable, as the $c_{a,b}$ must be either zero or infinite. Building on the discussion in Ref. [47], the displacement within the bandgap of the locally resonant metamaterial takes the form $U \propto e^{-\beta x}$, with the dimensionless wavenumber $k_x = \alpha + i\beta$. At the local resonance frequency, the imaginary part of the wavenumber (β) becomes infinite due to the divergent effective mass. Therefore, if the topological in-gap states are positioned within the singularity ($\beta \mapsto \infty$), this singular edge state becomes highly localized on scales comparable to single metamaterial units. To explore wave localization in a finite chain, we quantify localization using the inverse participation ratio (IPR), defined as $(\sum_{n=1}^m u_n^4)/(\sum_{n=1}^m u_n^2)^2$. We then calculate the IPR by tracking only topological gap states in the parametric space of the bi-frequency resonance [see Fig. 3(g)]. As the system transitions through the topological gap from BG to LRG, a remarkably high IPR is observed. Notably, the IPR reaches 1 near the centerline of the LRG regimes, indicating wave localization within a single unit cell, as previously argued, i.e., singular edge states.

Experimental realization.—Our objective is to experimentally demonstrate the conversion from a conventional edge state to a singular edge state through a topological gap transition. Therefore, the experimental approach requires a tunable local resonance. Depending on the building blocks of the metamaterial, local resonance may

appear as open pillars [48], Helmholtz resonators [7, 49], or engineered systems [4, 50]. However, directly mapping the structural levels of the local resonators to the proposed theoretical spring-mass model poses a challenge.

To that end, we utilize locally resonant granular crystals known as woodpile metamaterials [51, 52], composed of slender cylindrical beams [see Fig. 4(a)]. What makes this system special is that the resonator is “intrinsic”, in that local modes stem directly from the beams themselves [Fig. 4(b)]. Upon coupling with external perturbation and internal resonance, this system exhibits a local resonance effect. Thus, by adjusting the length of the cylinders, one can tune the associated internal vibrational frequency. The interaction potential between neighboring cells is determined by the nature of the contact [53]. Highly tunable, these metamaterials offer a platform for demonstrating various wave physics phenomena within the same system [51, 54]. The discretization of continuous cells (single cylinder) is achieved using physics-informed discrete element modeling (DEM) [55], resulting in unit cells that possess multiple local resonances [see Fig. 4(b)]. This mathematical model emerges from integrating the dispersion physics of lattice dynamics with the free vibration of continuum beam theory [see Ref. [43], Sec. IV for detailed mathematical modeling]. Therefore, given the geometries and material properties of the cylinders, we can analytically determine and tune the properties of the local resonators.

For chains with bi-local resonance frequencies, we construct a unit cell with two different cylinder lengths while maintaining the inversion symmetry. Under the exter-

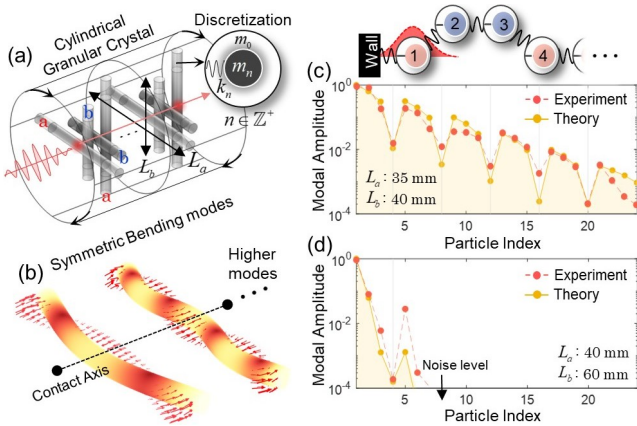


FIG. 4. Experimental realization of topologically protected singular edge states in a locally resonant granular-based metamaterial. (a) Schematic of the experimental platform consisting of slender cylindrical beams. The continuum unit cell (a single beam) is analytically mapped to a spring-mass unit cell consisting of multiple harmonic oscillators. (b) Mode shape of bending vibrational modes of cylindrical beams, which exhibit strong coupling to external excitation (i.e., the local resonance effect). (c)-(d) Mode profile of topological (boundary) edge states with the BG and LRG as references, respectively (logarithmic scale). The extracted experimental data (red markers) match the results of the eigenanalysis (yellow markers).

nal excitations, the wave field within the chain is detected using a non-contact laser Doppler vibrometer [see Ref. [43], Sec. III for the detailed experiment]. Through the eigenanalysis of DEM, we chose the beam lengths L_a and L_b such that the topological edge states emerged in either the BG or LRG (i.e., the presence or absence of gap transition). Within the designed setup, we observed the topological edge state within the BG [see Fig. 4(b)], where edge states extend throughout the chain [IPR = 0.427 (theory) and 0.476 ± 0.008 (experiment)]. This topological mode profile clearly agrees with the analysis results we got from the DEM. We now induce a topological gap transition by adjusting the local resonance. In this way, as shown in Fig. 4(d), we can observe highly localized topological edge states (on a logarithmic scale) within the initial part of the chain. For the current configuration, the IPR was calculated to be 0.992 (theory) and 0.975 ± 0.006 (experiment). The modal amplitude of the remaining part of the chain in experimental conditions shows noise from the experimental environment (see Ref. [43], Sec. V). In this way, we are able to demonstrate our topological singular edge states—highly localized waves within a unit cell—through the topological and gap transition. In addition, theoretical and experimental results of the topological interface states between topologically distinct systems can be found in Ref. [43], Fig. S5, and Sec. VI. The topological mode shape of the physical chain obtained through finite element analysis

is detailed in Sec. VII.

Conclusion.—In this work, we proposed topologically protected singular edge states in locally resonant metamaterials. Such states are distinct from conventional edge states due to their bandgap nature. We revealed a mechanism by which the singular edge state emerges through a gap transition from the Bragg-induced gap (BG) to the local resonance gap (LRG), along with a topological phase transition. Using the highly tunable granular-based metamaterials, we experimentally captured the distinct differences in topological edge states—highlighted by wave localization—between the BG and the LRG. Our findings suggest the extended scope of topological metamaterials, leveraging their inherent bandgap nature, with the potential for further expansion into higher-dimensional systems. While our experimental platform was performed in an elastic wave field, we believe that the fundamental physics presented can be extended to diverse domains exhibiting local resonance behaviors, such as acoustics, plasmonics, and photonics.

* These authors contributed equally to this work.

† eunhokim@jbnu.ac.kr

‡ jrsho@postech.ac.kr

- [1] J. J. Park, K. J. B. Lee, O. B. Wright, M. K. Jung, and S. H. Lee, *Physical Review Letters* **110**, 10.1103/physrevlett.110.244302 (2013).
- [2] R. Liu, Q. Cheng, T. Hand, J. J. Mock, T. J. Cui, S. A. Cummer, and D. R. Smith, *Physical Review Letters* **100**, 10.1103/physrevlett.100.023903 (2008).
- [3] D. R. Smith, J. B. Pendry, and M. C. K. Wiltshire, *Science* **305**, 788–792 (2004).
- [4] Z. Liu, X. Zhang, Y. Mao, Y. Y. Zhu, Z. Yang, C. T. Chan, and P. Sheng, *Science* **289**, 1734–1736 (2000).
- [5] N. I. Zheludev and Y. S. Kivshar, *Nature Materials* **11**, 917–924 (2012).
- [6] S. A. Cummer, J. Christensen, and A. Alù, *Nature Reviews Materials* **1**, 10.1038/natrevmats.2016.1 (2016).
- [7] G. Ma and P. Sheng, *Science Advances* **2**, 10.1126/sciadv.1501595 (2016).
- [8] N. Kaina, F. Lemoult, M. Fink, and G. Lerosey, *Nature* **525**, 77–81 (2015).
- [9] S. Yves, R. Fleury, T. Berthelot, M. Fink, F. Lemoult, and G. Lerosey, *Nature Communications* **8**, 10.1038/ncomms16023 (2017).
- [10] M. Z. Hasan and C. L. Kane, *Reviews of Modern Physics* **82**, 3045–3067 (2010).
- [11] X.-L. Qi and S.-C. Zhang, *Reviews of Modern Physics* **83**, 1057–1110 (2011).
- [12] A. Bansil, H. Lin, and T. Das, *Reviews of Modern Physics* **88**, 10.1103/revmodphys.88.021004 (2016).
- [13] E. Prodan and H. Schulz-Baldes, *Bulk and Boundary Invariants for Complex Topological Insulators: From K-Theory to Physics* (Springer International Publishing, 2016).
- [14] R. Süsstrunk and S. D. Huber, *Science* **349**, 47–50 (2015).

- [15] L. M. Nash, D. Kleckner, A. Read, V. Vitelli, A. M. Turner, and W. T. M. Irvine, *Proceedings of the National Academy of Sciences* **112**, 14495–14500 (2015).
- [16] M. Serra-Garcia, V. Peri, R. Süsstrunk, O. R. Bilal, T. Larsen, L. G. Villanueva, and S. D. Huber, *Nature* **555**, 342–345 (2018).
- [17] J. Cha, K. W. Kim, and C. Daraio, *Nature* **564**, 229–233 (2018).
- [18] P. Wang, L. Lu, and K. Bertoldi, *Physical Review Letters* **115**, 10.1103/physrevlett.115.104302 (2015).
- [19] J. Vila, R. K. Pal, and M. Ruzzene, *Physical Review B* **96**, 10.1103/physrevb.96.134307 (2017).
- [20] M. Xiao, G. Ma, Z. Yang, P. Sheng, Z. Q. Zhang, and C. T. Chan, *Nature Physics* **11**, 240–244 (2015).
- [21] C. L. Kane and T. C. Lubensky, *Nature Physics* **10**, 39–45 (2013).
- [22] R. K. Pal and M. Ruzzene, *New Journal of Physics* **19**, 025001 (2017).
- [23] S. H. Mousavi, A. B. Khanikaev, and Z. Wang, *Nature Communications* **6**, 10.1038/ncomms9682 (2015).
- [24] D. Z. Rocklin, B. G. Chen, M. Falk, V. Vitelli, and T. Lubensky, *Physical Review Letters* **116**, 10.1103/physrevlett.116.135503 (2016).
- [25] R. Chaunsali, C.-W. Chen, and J. Yang, *Physical Review B* **97**, 10.1103/physrevb.97.054307 (2018).
- [26] H. Xue, Y. Yang, and B. Zhang, *Nature Reviews Materials* **7**, 974–990 (2022).
- [27] J. K. Asbóth, L. Oroszlány, and A. Pályi, *A Short Course on Topological Insulators* (Springer International Publishing, 2016).
- [28] T. Ozawa, H. M. Price, A. Amo, N. Goldman, M. Hafezi, L. Lu, M. C. Rechtsman, D. Schuster, J. Simon, O. Zeitlinger, and I. Carusotto, *Reviews of Modern Physics* **91**, 10.1103/revmodphys.91.015006 (2019).
- [29] H. Yasuda, P. R. Buskohl, A. Gillman, T. D. Murphey, S. Stepney, R. A. Vaia, and J. R. Raney, *Nature* **598**, 39–48 (2021).
- [30] S. D. Huber, *Nature Physics* **12**, 621–623 (2016).
- [31] F. Zangeneh-Nejad and R. Fleury, *Nature Communications* **10**, 10.1038/s41467-019-10086-3 (2019).
- [32] H. Pirie, S. Sadhuka, J. Wang, R. Andrei, and J. E. Hoffman, *Physical Review Letters* **128**, 10.1103/physrevlett.128.015501 (2022).
- [33] D. Zhao, M. Xiao, C. W. Ling, C. T. Chan, and K. H. Fung, *Physical Review B* **98**, 10.1103/physrevb.98.014110 (2018).
- [34] Z.-w. Li, X.-s. Fang, B. Liang, Y. Li, and J.-c. Cheng, *Physical Review Applied* **14**, 10.1103/physrevapplied.14.054028 (2020).
- [35] A. Coutant, V. Achilleos, O. Richoux, G. Theocharis, and V. Pagneux, *The Journal of the Acoustical Society of America* **151**, 3626–3632 (2022).
- [36] D. Zhao, X. Chen, P. Li, and X.-F. Zhu, *AIP Advances* **11**, 10.1063/5.0034811 (2021).
- [37] A. Foehr, O. R. Bilal, S. D. Huber, and C. Daraio, *Physical Review Letters* **120**, 10.1103/physrevlett.120.205501 (2018).
- [38] T. Lee and H. Iizuka, *Physical Review B* **99**, 10.1103/physrevb.99.064305 (2019).
- [39] L. Fan, Y. Chen, S. An, T. Liu, H. Fan, J. Zhu, and Z. Su, *Physical Review Applied* **19**, 10.1103/physrevapplied.19.034065 (2023).
- [40] Z. Zhang, Y. Cheng, X. Liu, and J. Christensen, *Physical Review B* **99**, 10.1103/physrevb.99.224104 (2019).
- [41] Z.-Q. Jiao, S. Longhi, X.-W. Wang, J. Gao, W.-H. Zhou, Y. Wang, Y.-X. Fu, L. Wang, R.-J. Ren, L.-F. Qiao, and X.-M. Jin, *Physical Review Letters* **127**, 10.1103/physrevlett.127.147401 (2021).
- [42] S. Longhi, *Optics Letters* **43**, 4639 (2018).
- [43] See supplemental material at (url to be updated) for detailed descriptions of the theoretical model of inversion-symmetric extended ssh chain, effective hamiltonian based on perturbative theory, effective mass density, topological phase map, spectral ordering, experiment setup, discretization model, experimental bg vs. lrg, and finite element analysis, which includes refs. [51,53-55].
- [44] L. Fu and C. L. Kane, *Physical Review B* **76**, 10.1103/physrevb.76.045302 (2007).
- [45] *Proceedings of the Royal Society of London. Series A, Containing Papers of a Mathematical and Physical Character* **117**, 610–624 (1928).
- [46] P. B. Allen, S. Aubin, and R. B. Doak, *American Journal of Physics* **68**, 228–231 (2000).
- [47] H. Huang, C. Sun, and G. Huang, *International Journal of Engineering Science* **47**, 610–617 (2009).
- [48] A. Colombi, P. Roux, S. Guenneau, P. Gueguen, and R. V. Craster, *Scientific Reports* **6**, 10.1038/srep19238 (2016).
- [49] S. H. Lee, C. M. Park, Y. M. Seo, Z. G. Wang, and C. K. Kim, *Physical Review Letters* **104**, 10.1103/physrevlett.104.054301 (2010).
- [50] P. Wang, F. Casadei, S. Shan, J. C. Weaver, and K. Bertoldi, *Physical Review Letters* **113**, 10.1103/physrevlett.113.014301 (2014).
- [51] E. Kim, F. Li, C. Chong, G. Theocharis, J. Yang, and P. Kevrekidis, *Physical Review Letters* **114**, 10.1103/physrevlett.114.118002 (2015).
- [52] E. Kim and J. Yang, *Journal of the Mechanics and Physics of Solids* **71**, 33–45 (2014).
- [53] K. L. Johnson, *Contact Mechanics* (Cambridge University Press, 1985).
- [54] C. Chong, M. A. Porter, P. G. Kevrekidis, and C. Daraio, *Journal of Physics: Condensed Matter* **29**, 413003 (2017).
- [55] Y. Jang, E. Kim, J. Yang, and J. Rho, *Applied Mathematical Modelling* **125**, 571–590 (2024).

ACKNOWLEDGEMENTS

This work was financially supported by the POSCO-POSTECH-RIST Convergence Research Center program funded by POSCO and the National Research Foundation (NRF) grant (RS-2024-00356928) funded by the Ministry of Science and ICT (MSIT) of the Korean government, and the grant (PES4400) from the endowment project of “Development of smart sensor technology for underwater environment monitoring” funded by Korea Research Institute of Ships Ocean engineering (KRISO). E.K. also acknowledges the support of the National Research Foundation grant (NRF-2020R1A2C2013414) and the Commercialization Promotion Agency for R&D Outcomes (COMPA) grant (RS-2023-00304743) funded by the Korean Government (Ministry of Science and ICT, 2023).